Impedance Modeling and Stability Analysis of Grid-Connected DFIG-based Wind Farm with a VSC-HVDC

Sun, Kun; Yao, Wei; Fang, Jiakun; Ai, Xiaomeng; Wen, Jinyu; Cheng, Shijie

Published in:
IEEE Journal of Emerging and Selected Topics in Power Electronics

DOI (link to publication from Publisher):
10.1109/JESTPE.2019.2901747

Publication date:
2020

Document Version
Accepted author manuscript, peer reviewed version

This article has been accepted for publication in a future issue of this journal, but has not been fully edited. Content may change prior to final publication. Citation information: DOI 10.1109/JESTPE.2019.2901747, IEEE Journal of Emerging and Selected Topics in Power Electronics

Impedance Modeling and Stability Analysis of Grid-Connected DFIG-based Wind Farm with a VSC-HVDC

Kun Sun, Wei Yao, *Senior Member, IEEE*, Jiakun Fang, *Member, IEEE*, Xiaomeng Ai, *Member, IEEE*, Jinyu Wen, *Member, IEEE*, Shijie Cheng, *Life Fellow, IEEE*

***Abstract*—A new type of subsynchronous oscillation (SSO) has been observed recently in double fed induction generator (DFIG)-based wind farm integrated via voltage source converter based HVDC (VSC-HVDC) system. However, the mechanism of this emerging oscillation is not entirely understood. In this paper, the impedance models of DFIG with and without considering the phase locked loop (PLL) dynamics are both derived. Then the impedance-based simplified equivalent circuit of the multiple DFIGs interfaced with VSC-HVDC system is established. This model can be further represented as the RLC series resonance circuit to quantify the start-oscillating condition intuitively. The theoretical analysis results show that DFIGs behave as an inductance in series with a negative resistance at the resonance point, whose interaction with wind farm side VSC (WFVSC) (regard as a resistance-capacitance) constitutes an equivalent RLC resonance circuit with negative resistance. Therefore, the oscillation tends to occur due to the negative damping. In addition, the impact of various factors including number of grid-connected DFIG-wind turbines, wind speed, and parameters of PI controllers and PLL on the SSO characteristics are analyzed based on the proposed simplified model. Finally, the correctness of the theoretical analysis is validated by both the time-domain simulation and hardware-in-loop (HIL) experiments.**

***Index Terms*—DFIG; VSC-HVDC; subsynchronous oscillation; impedance-based method; phase locked loop; wind farm.**

NOMENCLATURE

$\boldsymbol{U_s}, \boldsymbol{U_r}$	Stator and rotor voltage vector.
$\boldsymbol{I_s}, \boldsymbol{I_r}$	Stator and rotor current vector.
$\boldsymbol{\psi_s}, \boldsymbol{\psi_r}$	Stator and rotor flux linkage vector.
P_s, P_r	Stator and rotor active power.
L_{ss}, L_{rr}	Stator and rotor inductances in dq frame.
L_s, L_r	Stator and rotor inductances in abc frame.
r_s, r_r	Stator and rotor resistance.
L_m	Magnetizing inductance.
L_g	Filter inductance of grid-side converter (GSC).
v_c, i_c	Output voltage and current of WFVSC.
v_o	Grid terminal voltage of WFVSC.
L_f, C_f	Filter inductance and capacitance of WFVSC.
L_l, r_l	Inductance and resistance of line and transformers.
ω_1	Synchronous angular frequency.
$\theta_{pll}, \omega_{pll}$	PLL output angle and angular frequency.
θ_r, ω_r	Rotor angle and angular frequency.
n	Number of grid-connected DFIG-WTs.
$H_\omega(s), H_Q(s)$	Rotor-side converter (RSC) speed and reactive power controller.
$H_s(s)$	GSC dc voltage controller.
$H_r(s), H_g(s)$	RSC and GSC current controller.
$H_{pll}(s)$	PLL controller.
$H_v(s), H_c(s)$	WFVSC voltage and current controller.
K_{pr}, K_{ir}	Proportional and integral gains of $H_r(s)$.
K_{dr}, K_{dg}	Decoupling gain of $H_r(s)$ and $H_g(s)$.
K_{pv}, K_{iv}	Proportional and integral gains of $H_v(s)$.
K_{pc}, K_{ic}	Proportional and integral gains of $H_c(s)$.
K_{ppll}, K_{ipll}	Proportional and integral gains of $H_{pll}(s)$.

Superscript

pll	Variables measured in controller frame.

Subscripts

d, q	D- and q-axis components in dq frame.
s, r	Stator and rotor components.
c	WFVSC components.

Manuscript submitted September 25, 2018; revised December 28, 2018; accepted February 22, 2019. This work was supported by National Natural Science Foundation of China under Grant 51577075. Paper no. JESTPE-2018-09-0757 *(Corresponding author: Wei Yao.)*

K. Sun, W. Yao, X. M. Ai, J. Y. Wen, and S. J. Cheng are with State Key Laboratory of Advanced Electromagnetic Engineering and Technology, School of Electrical and Electronic Engineering, Huazhong University of Science and Technology, Wuhan, 430074, China. (e-mail: kunsun93@foxmail.com; w.yao@hust.edu.cn; xiaomengai@hust.edu.cn; jinyu.wen@hust.edu.cn; sjcheng@hust.edu.cn)

J. K. Fang is with Department of Energy Technology, Aalborg University Aalborg, DK9220, Denmark. (email: jfa@et.aau.dk).

I. INTRODUCTION

With the growth of the installed wind power capacity worldwide, the bulk wind power transmission is in desperate need of a suitable solution. It is generally agreed that the VSC-HVDC technology is a promising option for grid integration of bulk wind powers [1], [2]. For instance, VSC-HVDC will be applied to delivering the bulk wind power in Northwest China to the load centers located at the eastern

This article has been accepted for publication in a future issue of this journal, but has not been fully edited. Content may change prior to final publication. Citation information: DOI 10.1109/JESTPE.2019.2901747, IEEE Journal of Emerging and Selected Topics in Power Electronics

coast. However, the stability of the wind farm connected through VSC-HVDC system is of particular concern since the lack of direct connection to a strong ac grid at the point of common coupling (PCC) [3]. The potential oscillation problem may be induced and intensified by the power electronic devices due to their fast response [4], [5]. The SSO around 20 Hz has occurred in a VSC-HVDC transmission demonstration project in China when DFIG-based wind farm integrated, which results in outage of the wind farm [6], [7]. This is a new power oscillation phenomenon, whose mechanism is different from that between wind farm and series-compensation or LCC-HVDC. It may result from the interaction between wind farm and VSC-HVDC.

The significant efforts have been devoted to the stability of grid-connected DFIG and VSC-HVDC system respectively. For instance, the impedance model for DFIG interfaced with series-compensated grid is developed in [8]–[10]. And the impact of various parameters on the characteristics of SSO including compensation level, wind speed and RSC control parameters are investigated. In [11], the impact of the number of grid-connected DFIG-wind turbines on SSO is also analyzed using the basic equivalent circuit model of DFIG. However, this research is incomplete since the detail modeling process of DFIG and the graphic analysis of the SSO mechanism are lacking. In [12], an open-loop SSO modal resonance caused by DFIGs is investigated using the modal analysis based on a closed-loop interconnected model of the system. However, this resonance mainly origins from the reactive current PI controller mode of DFIG, which has little correlation with other parameters. Besides, none of the above references consider the integration of DFIG through the VSC-HVDC system. Thus, the feasibility of the proposed methods and conclusions of the above references need to be retested when the VSC-HVDC system is taken into account. The analytical impedance models from [13]–[15] also provide approaches to characterize the effects of different circuit and control parameters on stability of VSC-HVDC system. In addition, the SSO phenomenon between PMSG-based wind farm and VSC-HVDC system is reported in [16], [17] recently. However, few references have investigated the interaction between DFIG-based wind farm and VSC-HVDC system in-depth. In [18], [19], the eigenvalue analysis of the DFIG-based wind farm connected to VSC-HVDC system is conducted to assess the possible resonances and system stability. However, the mechanism of the resonances is not revealed. In [3], the interaction between DFIG and VSC-HVDC system is analyzed using the internal voltage phase motion equation. However, the effect of the dynamics of the current loops is neglected. In [20], the impact of low frequency series resonances on the voltage stability of the similar system is discussed, but the resonances in the subsynchronous frequency region are not concerned. In [21], the SSO existing in the DFIG-based wind farm connected to VSC-HVDC system is analyzed by the impedance-based method. However, only GSC is considered in the modeling with RSC ignored, which means the dynamic of DFIG may not be exactly represented. Noticeably, none of the above literature consider the influence of PLL of the DFIG on the SSO characteristics. References [22]–[25] find that the PLL dynamic can affect the output impedance of grid-connected converter. And [26] reveals that the influence of PLL is the critical factor of the negative damping in a grid-connected VSC system. However, the PLL dynamic in DFIG may affect the system damping in a different way. Therefore, the influence of PLL in DFIG on the SSO characteristics is worthy to be further investigated.

Currently, the impedance-based method is demonstrated suitable for the new power oscillation problem caused by the interaction between grid-connected units [22], [24]. The impedance-based method has the following advantages: the output characteristics of units can be intuitively expressed in the impedance form; the stability criterion is simple and concise; the extension of topology is convenient [22]. In addition, the output characteristics of units can be well controlled by adjusting the parameters and then the resonant point can be avoided. The dq frame impedance modeling is proposed at first by the small-signal linearization in a steady-state dc operation point in dq frame [27]. However, the dq impedance is complex to measure and the stability criterion is complicated. Consequently, the harmonic linearization method is proposed to build the sequence impedance model of the units which is convenient for measurement and has clear physical meaning [28].

In this paper, the simplified impedance-based equivalent circuit of the system is proposed to investigate the mechanism and characteristics of SSO event in the grid-connected DFIG-based wind farm through VSC-HVDC system. Then the stability criterion of SSO is derived based on the RLC resonance circuit. The reasonable mechanism for SSO is also induced, and the factors influencing the SSO characteristics are further studied. Moreover, the influence of PLL parameters on SSO is also quantified by deriving the impedance model of DFIG considering the PLL dynamics. Finally, the correctness of the theoretical analysis results is validated by both the time-domain simulation and HIL experiments.

The main contributions of this paper are summarized as follows:

- The potential SSO risk of the DFIG-based wind farm integrated to power grid through VSC-HVDC system is investigated. This is a new type of oscillation whose origin is the control interaction between DFIG and VSC-HVDC. The impedance models of DFIG with and without considering the PLL dynamics are both derived.
- To simplify the analysis of the SSO characteristics, the simplified models of DFIG and WFVSC are built. And then the simplified equivalent circuit of the multiple DFIGs interfaced with VSC-HVDC system is proposed. This simplified model can be further represented as a RLC series resonance circuit to quantify the start-oscillating condition intuitively.
- The influence factors including the number of DFIG-WTs, wind speed, and parameters of PI controllers on SSO characteristic are analyzed comprehensively according to the proposed simplified model. Besides, the effect of PLL parameters is also studied by the impedance model of DFIG with PLL. The correctness of the theoretical analysis results is validated by both the time domain

This article has been accepted for publication in a future issue of this journal, but has not been fully edited. Content may change prior to final publication. Citation information: DOI 10.1109/JESTPE.2019.2901747, IEEE Journal of Emerging and Selected Topics in Power Electronics

simulation and HIL experiments.

The rest of this paper is organized as follows. The SSO characteristic of the test system is investigated in Section II. Section III derives the impedance model of DFIG and WFVSC, and then the impedance-based simplified equivalent circuit of the system is proposed. In Section IV, the stability criterion of SSO is represented, and the impact of various factors on the SSO characteristics is analyzed. Section V and Section VI validate the correctness of the theoretical analysis by simulation and HIL experiments, respectively. Finally, conclusions are drawn in Section VII.

II. SSO Characteristics of System

The configuration of the test system is briefly introduced firstly. Then time-domain simulations and spectrum analysis are conducted to prove the existence of SSO in the test system.

A. System Configuration

The test system shown in Fig. 1 consists of five wind farms, each with a capacity of 50 MW. The wind power is collected by 35 kV AC bus and connected to a centralized step-up station. With a little local load near the wind farms, the wind power is then stepped up to 110 kV and transmitted through VSC-HVDC system to the grid. The rated capacity of the DFIG-WTs in these wind farms are 1.5 MW. And all of the grid-connected DFIGs run in the maximum power point tracking (MPPT) mode. To simplify the system model, the equivalent aggregated model of DFIGs used in [29], [30] is adopted since we focus on the interaction between DFIGs and VSC-HVDC instead of the internal action among DFIGs. The rated voltage is 110 kV and the rated frequency is 50 Hz. R_{L} and X_{L} are the impedance of the transmission line. Z_{L} represents the load disturbance. The other parameters of the system are listed in the Appendix.

B. SSO Phenomenon under Different Operating Conditions

A detailed electromagnetic transient model of the test system shown in Fig. 1 is established with switching device model of the VSC-HVDC and the drive-train of the DFIG in the Matlab/Simulink environment associated with the SimPowerSystems Blockset. The following two typical scenarios are presented as follows.

1) Scenario 1: In this scenario, the dynamics of SSO following a step change of the number of the grid-connected DFIG-WTs is investigated. Initially, there are 100 grid-connected DFIG-WTs in the five existing wind farms. When multiple DFIGs are considered, it is assumes that all the turbines operate under the same condition of wind speed at 8.5 m/s (rotating speed at 0.9 pu). To meet the growing demand for electric load, a new wind farm has been built. At t=15 s, 20 more turbines in the new wind farm are integrated into the system. Fig. 2(a) shows the active power of the wind farms. It can be found that once additional 20 DFIG-WTs are synchronized at 15 s, the unstable power oscillation emerges.

2) Scenario 2: In this scenario, the relationship between the dynamics of SSO and the wind speed is investigated. Initially, there are 100 grid-connected DFIG-WTs operating under the same condition of wind speed at 9.5 m/s (rotating speed at 1.0 pu). During 10 $\sim$ 20 s, the wind speed decreases gradually from 9.5 m/s to 7.5 m/s at the speed of -0.2 m/s. Fig. 2(b) shows the active power of the wind farms. It can be found that the power oscillation emerges with the decrease of wind speed and it is sustained with even higher amplitude.

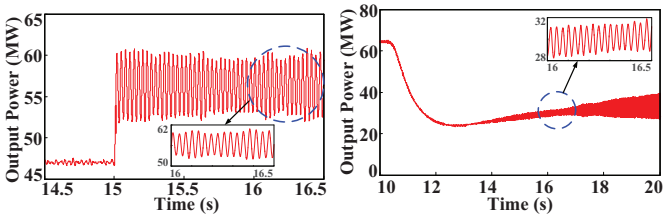

(a) (b)

Fig. 2. SSO Phenomenon under different operating conditions: (a) Increase of the number of the grid-connected DFIG-WTs, (b) Decrease of wind speed.

C. Spectrum Analysis of SSO

It can be concluded that SSO may occur with the number increase of grid-connected DFIG-WTs or the wind speed decrease. In particular, Scenario 1 in Section II-B is considered as an example to investigate the characteristics of SSO. As shown in Fig. 3, the curves of d-axis rotor current, active power of a single WTG, phase-A current on PCC and the dc current of VSC-HVDC system are depicted during 14.5 s to 16.5 s. Clearly, all the observed signals become unstable immediately after the step raise of the number of DFIGs. Moreover, this oscillation is moving towards the main power grid through VSC-HVDC system, which may lead to the power fluctuations of the power grid.

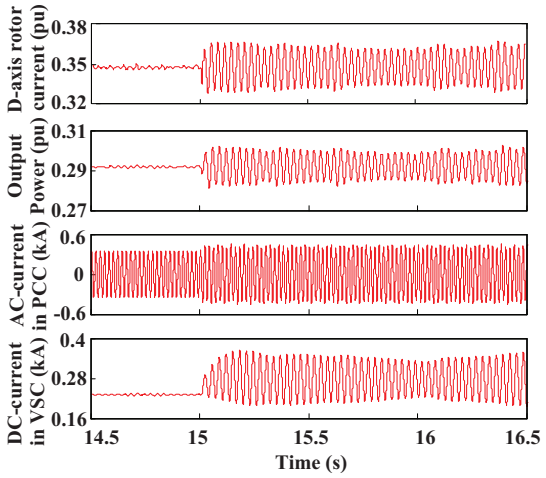

Fig. 3. Dynamics of wind farms and VSC-HVDC: (a) D-axis current of RSC, ird. (b) Active power of a single turbine. (c) Phase-A current on the PCC. (d) Dc current of VSC-HVDC.

Discrete Fourier transform (DFT) is applied for the spectrum analysis of the current and the active power on PCC in Scenario 1. As shown in Fig. 4, the current contains a subsynchronous component at 17.1 Hz, while the active power

This article has been accepted for publication in a future issue of this journal, but has not been fully edited. Content may change prior to final publication. Citation information: DOI 10.1109/JESTPE.2019.2901747, IEEE Journal of Emerging and Selected Topics in Power Electronics

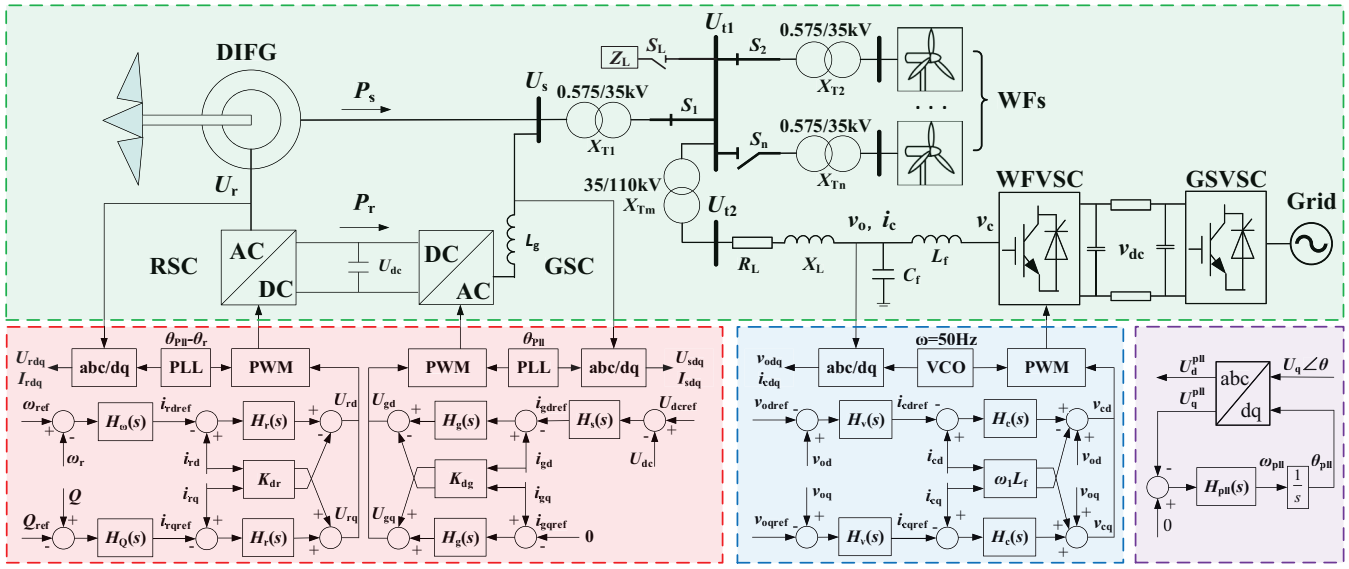

Fig. 1. System diagram and control scheme of the test system: DFIGs interfaced with VSC-HVDC system.

contains a subsynchronous component at 32.9 Hz. It should be noted that the oscillating frequency in abc frame complements the oscillating frequency in dq frame (the sum of them is equal to synchronous frequency). That means the system has an unstable mode with 17.1 Hz frequency and has oscillatory behavior caused by the interaction between DFIG and VSC-HVDC. The mechanism explanation and the characteristics analysis of this oscillation will be clearly illustrated in Section IV.

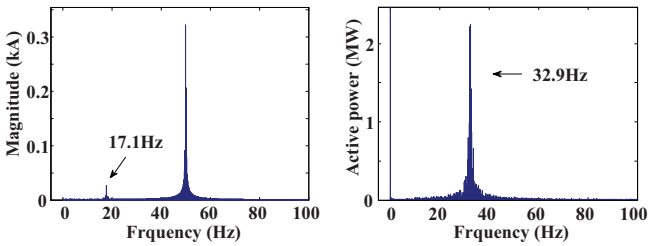

(a) (b)

Fig. 4. Spectrum analysis: (a) Phase-A current on the PCC, (b) Active power of wind farms.

III. System Modeling and Control

In this section, the impedance model of DFIG and WFVSC are derived. Since the model is normally established in a way from simple to complex, the DFIG model without PLL is developed at first, and then the DFIG model with PLL will be derived. Thereafter the impedance-based simplified equivalent circuit of the investigated system is established for the mechanism analysis of SSO.

A. Impedance Model of DFIG

1) Model Without Considering PLL [9]–[11]*:* The control structure of DFIG is depicted in Fig. 1. The controllers of RSC and GSC are based on dq reference frame, in which the d-axis is orientated to the stator voltage vector. RSC and GSC both include two cascade control loops. The outer control loops are associated with power controls while the inner control loops are current controls. Typical PI controllers are applied in the control loops. Specifically, RSC realizes the independent control of the active and reactive power flowing between the stator and the grid. GSC aims at keeping the dc-voltage constant and controlling the reactive power. The q-axis reference current of GSC is often set to zero.

The variables such as voltage, current and flux linkage can be expressed in the complex space vector form (eg., $\boldsymbol{U}=U_{\mathrm{d}}+jU_{\mathrm{q}},\boldsymbol{I}=i_{\mathrm{d}}+ji_{\mathrm{q}},\boldsymbol{\psi}=\psi_{\mathrm{d}}+j\psi_{\mathrm{q}}$) for the sake of brevity. Thus, the winding flux linkage equation and voltage equation of DFIG in dq frame can be presented as follows:

$$\begin{cases}\boldsymbol{\psi}_{\mathbf{s}}=L_{\mathrm{ss}}\boldsymbol{I}_{\mathbf{s}}+L_{\mathrm{m}}\boldsymbol{I}_{\mathbf{r}}\\ \boldsymbol{\psi}_{\mathbf{r}}=L_{\mathrm{rr}}\boldsymbol{I}_{\mathbf{r}}+L_{\mathrm{m}}\boldsymbol{I}_{\mathbf{s}}\end{cases}\tag{1}$$

$$\begin{cases}\boldsymbol{U}_{\mathbf{s}}=r_{\mathrm{s}}\boldsymbol{I}_{\mathbf{s}}+\dfrac{d\boldsymbol{\psi}_{\mathbf{s}}}{dt}+j\omega_1\boldsymbol{\psi}_{\mathbf{s}}\\ \boldsymbol{U}_{\mathbf{r}}=r_{\mathrm{r}}\boldsymbol{I}_{\mathbf{r}}+\dfrac{d\boldsymbol{\psi}_{\mathbf{r}}}{dt}+j(\omega_1-\omega_{\mathrm{r}})\boldsymbol{\psi}_{\mathbf{r}}\end{cases}\tag{2}$$

where the positive current flows to the machine and produces the positive flux linkage.

By combining (1) and (2), the stator voltage vector $\boldsymbol{U}_{\mathbf{s}}$ can be expressed by $\boldsymbol{I}_{\mathbf{s}}$ and $\boldsymbol{U}_{\mathbf{r}}$ in Laplace domain. Therefore, the terminal characteristic of DFIG is described as:

$$\boldsymbol{U}_{\mathbf{s}}=\underbrace{\left[r_{\mathrm{s}}+(s+j\omega_1)\left(L_{\mathrm{ss}}-\frac{L_{\mathrm{m}}^2[s+j(\omega_1-\omega_{\mathrm{r}})]}{r_{\mathrm{r}}+[s+j(\omega_1-\omega_{\mathrm{r}})]L_{\mathrm{rr}}}\right)\right]}_{Z_{\mathrm{o}}(s)}\boldsymbol{I}_{\mathbf{s}}+\frac{(s+j\omega_1)L_{\mathrm{m}}}{r_{\mathrm{r}}+[s+j(\omega_1-\omega_{\mathrm{r}})]L_{\mathrm{rr}}}\boldsymbol{U}_{\mathbf{r}}\tag{3}$$

where s is the differential operator and $Z_{\mathrm{o}}(s)$ is the impedance of the induction machine in dq frame which can be obtained from (3).

However, the main circuit of DFIG is constructed in abc frame. Thus, for convenient analysis, $Z_{\mathrm{o}}(s)$ is transformed

This article has been accepted for publication in a future issue of this journal, but has not been fully edited. Content may change prior to final publication. Citation information: DOI 10.1109/JESTPE.2019.2901747, IEEE Journal of Emerging and Selected Topics in Power Electronics

into the positive sequence impedance which can be derived by replacing s with $(s-j\omega_1)$ [9].

$$Z_o(s) = r_s + s(L_s + L_r) + \frac{s}{s - j\omega_r} r_r \tag{4}$$

where $L_{ss} = L_s + L_m$ and $L_{rr} = L_r + L_m$. And (4) is simplified since the value of L_m is sufficiently large compared with other inductances.

Then the influence of RSC and GSC are taken into account. Note that the outer control loops are considered to be constant since the dynamic responses of them are much slower than that of the inner control loops, which means the outer control loops falls out of the SSO frequency range [31], [32]. Therefore, the influence of the outer loops of DFIG is not considered in this paper. The current control loops can also be expressed in the complex space vector form in abc frame.

$$\begin{cases} \boldsymbol{U_r} = H_r(s-j\omega_1)(\boldsymbol{I_{rref}} - \boldsymbol{I_r}) + jK_{dr}\boldsymbol{I_r} \\ \boldsymbol{U_s} = H_g(s-j\omega_1)(\boldsymbol{I_{gref}} - \boldsymbol{I_g}) + jK_{gr}\boldsymbol{I_s} \end{cases} \tag{5}$$

According to (5), RSC can be represented as a voltage source $\boldsymbol{I_{rref}}H_r(s-j\omega_1)$ in series with an impedance $Z_{rsc} = H_r(s-j\omega_1) - jK_{dr}$. And GSC can be represented as a voltage source $\boldsymbol{I_{gref}}H_g(s-j\omega_1)$ in series with an impedance $Z_{gsc} = H_g(s-j\omega_1) - jK_{gr}$. Thus, the equivalent circuit of DFIG is depicted in Fig. 5.

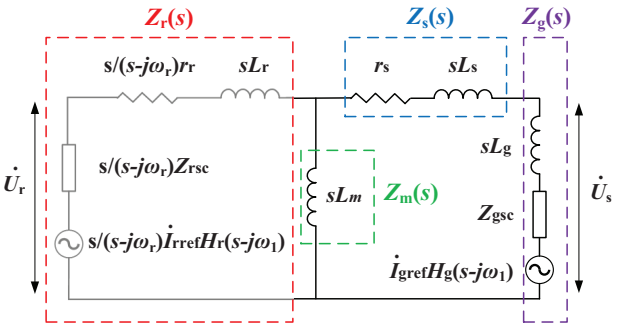

Fig. 5. The equivalent circuit of DFIG.

As shown in Fig. 5, $Z_r(s)$ is the sum of the rotor resistance, inductances and the equivalent impedance of RSC. $Z_s(s)$ is the sum of the stator resistance and inductances. $Z_g(s)$ is the sum of the equivalent impedance of GSC and its filter. $Z_m(s)$ is the excitation impedance.

2) Model With Considering PLL: The PLL dynamics is taken into account since SSO may be influenced by the PLL control parameters. However, the deduction process of impedance model of DFIG with the PLL unit in [33], [34] is hard to be understood since it does not contain an explicit physical meaning. Instead, to obtain the impedance model intuitively and conveniently, the method based on the equivalent circuit of DFIG with the PLL unit is proposed in this work.

Firstly the small-signal model of the PLL unit is presented [22]–[25]. The block diagram of the synchronous reference frame phase locked loop (SRF-PLL) in the converter of DFIG is shown in Fig. 1. PLL is used for phase tracking of the PCC voltage U_{pcc} and it can well synchronize the phase θ of U_{pcc} in a steady state. However, when U_{pcc} is disturbed by small-signal perturbations, θ cannot be synchronized accurately and an angle deviation $\Delta\theta$ is introduced due to the PLL dynamics. The relationship between the PLL output angle θ_{pll} and the actual value θ can be expressed as $\theta_{pll} = \theta + \Delta\theta$.

As shown in Fig. 6, the system has two dq frames during the transient process of PLL: one is the system dq frame which is defined by θ, and the other is the controller dq frame which is defined by θ_{pll}. The angle difference between these two dq frames is $\Delta\theta$. Note that the variables in the controller dq frame are denoted with the superscript 'pll'.

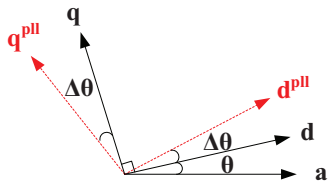

Fig. 6. The system dq frame and the controller dq frame.

As the control structure of the converter is established in the controller dq frame, small-signal perturbations to U_{pcc} can affect the output voltage and current of the converter since θ_{pll} is disturbed, and further influence the output impedance of DFIG. According to Fig. 1, the deviation $\Delta\theta$ of the PLL output angle can be expressed as:

$$\Delta\theta = \frac{1}{s} H_{pll} \Delta U_{pccq}^{pll} \tag{6}$$

According to [22]–[25], the disturbance relationship between a variable x in the controller dq frame and the system dq frame can be derived as follows:

$$\begin{cases} \Delta x_d^{pll} = \Delta x_d + x_q T_{pll}(s) \Delta U_{pccq} \\ \Delta x_q^{pll} = \Delta x_q - x_d T_{pll}(s) \Delta U_{pccq} \end{cases} \tag{7}$$

where the disturbance transfer function between the PLL output angle and q-component of the PCC voltage is expressed as the following equation:

$$T_{pll}(s) = \frac{\Delta\theta}{\Delta U_{pccq}} = \frac{H_{pll}(s)}{s + U_{pccd} H_{pll}(s)} \tag{8}$$

Note that the transformation by complex space vector is no longer applicable since the system is asymmetrical due to the effect of PLL. Therefore, the rotor voltage and current can be expressed in matrix form: $\mathbf{U_{rdq}} = [U_{rd}\ U_{rq}]^T$ and $\mathbf{I_{rdq}} = [i_{rd}\ i_{rq}]^T$. As the control structure of RSC is based on the controller dq frame, $\mathbf{U_{rdq}}$ and $\mathbf{I_{rdq}}$ are both influenced by PLL. Thus, the disturbance relationship of the rotor voltage and current between these two frames can be obtained according to (7). $\mathbf{G_{pll}^u}(s)$ represents the transform from the system voltage to voltage in the controller dq frame. $\mathbf{G_{pll}^i}(s)$ represents the transform from the system voltage to current in the controller dq frame.

$$\begin{cases} \Delta\mathbf{U_{rdq}^{pll}} = \Delta\mathbf{U_{rdq}} + \mathbf{G_{pll}^u}(s)\Delta\mathbf{U_{pccdq}} \\ \Delta\mathbf{I_{rdq}^{pll}} = \Delta\mathbf{I_{rdq}} + \mathbf{G_{pll}^i}(s)\Delta\mathbf{U_{pccdq}} \end{cases} \tag{9}$$

In order to model the small-signal propagation path through the PLL unit, the transfer function matrix $\mathbf{G_{pll}^u}(s)$ and $\mathbf{G_{pll}^i}(s)$ in (9) are defined after some proper simplifications. Firstly the voltage ratio between PCC voltage and stator winding voltage

This article has been accepted for publication in a future issue of this journal, but has not been fully edited. Content may change prior to final publication. Citation information: DOI 10.1109/JESTPE.2019.2901747, IEEE Journal of Emerging and Selected Topics in Power Electronics

is not considered here, thus the relationship between the rotor voltage, stator voltage and PCC voltage can be approximately expressed as $U_{rd} \approx U_{sd} = U_{pccd}$, $U_{rq} \approx U_{sq} = U_{pccq} = 0$. In addition, since the unity power factor control is adopted, q-component of the rotor current $i_{rq} \approx 0$. Moreover, as shown in Fig. 5, since $Z_g(s)$ is connected in parallel with the terminal of the circuit and its large magnitude in the subsynchronous frequency region, the influence of GSC branch can be ignored for SSO analysis [9]. And the excitation branch $Z_m(s)$ can also be neglected for the same reason. Thus, it can be found that $i_{rd} \approx i_{sd}$, $i_{rq} \approx i_{sq}$.

$$\begin{cases} \mathbf{G}^{u}_{\mathbf{pll}}(s) = \begin{bmatrix} 0 & 0 \\ 0 & -U_{rd}T_{pll}(s) \end{bmatrix} \\ \mathbf{G}^{i}_{\mathbf{pll}}(s) = \begin{bmatrix} 0 & 0 \\ 0 & -i_{rd}T_{pll}(s) \end{bmatrix} \end{cases} \tag{10}$$

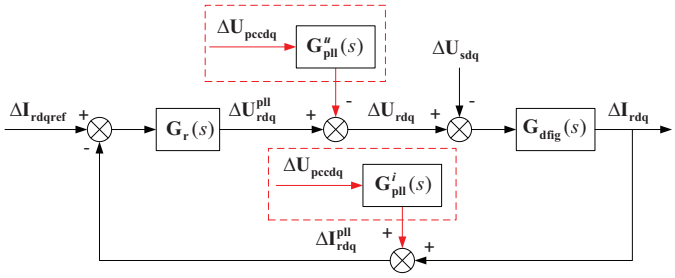

Fig. 7. Small-signal circuit model of the DFIG including PLL.

Then the influence of PLL is taken into account. By combining Fig. 5, (9) and (10), the small-signal circuit model of DFIG which is influenced by PLL is obtained and shown in Fig. 7. $\mathbf{G_{dfig}}(s)$ is the admittance of the induction machine; matrix $\mathbf{G_r}(s)$ is the transfer function of RSC current controller. $\mathbf{G_{dfig}}(s)$ and $\mathbf{G_r}(s)$ can be expressed as:

$$\mathbf{G_{dfig}}(s) = \left(\frac{r_r}{S_{lip}(s)} + sL_r + r_s + sL_s\right)^{-1} \tag{11}$$

$$\mathbf{G_r}(s) = \frac{1}{S_{lip}(s)} \begin{bmatrix} H_r(s) & -K_{dr} \\ K_{dr} & H_r(s) \end{bmatrix} \tag{12}$$

where the slip of rotor is expressed as $S_{lip}(s) = (s - j\omega_r)/s$. Since SSO issue is investigated in this paper, we focus on the rotor slip in the whole subsynchronous frequency range instead of the normal slip in the base frequency, which means the rotor slip is a variable and can be expressed as a transfer function.

According to Fig. 7, the rotor current in the transient process can be derived as:

$$\begin{aligned} \Delta\mathbf{I_{rdq}} = [\mathbf{G_r}(s)(\Delta\mathbf{I_{rdqref}} - \Delta\mathbf{I_{rdq}} - \mathbf{G^i_{pll}}(s)\Delta\mathbf{U_{pccdq}}) \\ - \mathbf{G^u_{pll}}(s)\Delta\mathbf{U_{pccdq}} - \Delta\mathbf{U_{sdq}}]\mathbf{G_{dfig}}(s) \end{aligned} \tag{13}$$

The disturbance relationship between the rotor current, rotor current reference and stator voltage can be derived according to (13), and then the output impedance of DFIG seen from the terminal is expressed as:

$$\begin{aligned} \mathbf{Z_{dq}}(s) &= (\mathbf{G_r}(s) + \mathbf{G_{dfig}}(s)^{-1})[\mathbf{I} + \mathbf{G^i_{pll}}(s)\mathbf{G_r}(s) + \mathbf{G^u_{pll}}(s)]^{-1} \\ &= \frac{\mathbf{G_r}(s) + \mathbf{G_{dfig}}(s)^{-1}}{\begin{bmatrix} 1 & 0 \\ 0 & 1 - (i_{rd}H_r(s)/S_{lip}(s) + U_{rd})T_{pll}(s) \end{bmatrix}} \end{aligned} \tag{14}$$

where $\mathbf{I}$ is second order identity matrix. The coefficient of the voltage term $(\mathbf{I} + \mathbf{G^i_{pll}}(s)\mathbf{G_r}(s) + \mathbf{G^u_{pll}}(s))$ involves the PLL unit information. Consequently, the output impedance of DFIG includes the equivalent impedance component which is regard as an additive result of the PLL performance. Note that the impedance of DFIG in dq frame is a 2×2 matrix which includes four components as follows:

$$\begin{cases} Z_{dd}(s) = \dfrac{r_r}{S_{lip}(s)} + sL_r + r_s + sL_s \\ Z_{dq}(s) = \dfrac{-K_{dr}}{S_{lip}(s)} \dfrac{1}{1 - (i_{rd}H_r(s)/S_{lip}(s) + U_{rd})T_{pll}(s)} \\ Z_{qd}(s) = \dfrac{-K_{dr}}{S_{lip}(s)} \\ Z_{qq}(s) = \dfrac{Z_{dd}(s)}{1 - (i_{rd}H_r(s)/S_{lip}(s) + U_{rd})T_{pll}(s)} \end{cases} \tag{15}$$

According to (15), it can be seen that the diagonal elements Z_{dd} and Z_{qq} reflect the main characteristics of the impedance of DFIG. Z_{dd} does not include the PLL unit information. In contrast, the denominator of Z_{qq} reflects the influence of PLL while the numerator of Z_{qq} equals to Z_{dd}. The off-diagonal elements Z_{dq} and Z_{qd} represent the coupling effect in the current control between d and q axis. Since the cross-coupling impedance Z_{dq} and Z_{qd} are very small due to the small value of K_{dr}, PLL has an effect mainly on q-axis impedance Z_{qq} [35]. Since $\mathbf{Z_{dq}}(s)$ is asymmetrical due to the effect of PLL, it can be transformed into the sequence impedance for the convenient analysis by the following equation [36]–[38]:

$$\mathbf{Z_{pn}}(s) = \begin{bmatrix} 1 & 1 \\ -j & j \end{bmatrix}^{-1} \mathbf{Z_{dq}}(s) \begin{bmatrix} 1 & j \\ 1 & -j \end{bmatrix} \tag{16}$$

The off-diagonal elements of the sequence impedance represent the coupling between the positive and the negative dominant frequency components. However, Z_{pn} and Z_{np} can be neglected in this study due to their small value. Therefore, the impedance model in (16) changes to a diagonal matrix with the diagonal elements Z_{pp} and Z_{nn}. Note that the difference between Z_{pp} and Z_{nn} only lies in the opposite sign of PLL output angle which is used in coordinate transformation [39]. This difference only affects the sign of the coupling terms in dq frame and affects mostly the positive-sequence impedance [33]. Therefore, the positive sequence impedance model of DFIG is adopted:

$$\begin{aligned} Z_{dfig}(s) = &\left(\frac{r_r + H_r(s - j\omega_1) - jK_{dr}}{S_{lip}(s)} + sL_r + r_s + sL_s\right) \\ &\left[\frac{1}{2}\left(1 + \frac{1}{1 - (i_{rd}H_r(s - j\omega_1)/S_{lip}(s) + U_{rd})T_{pll}(s - j\omega_1)}\right)\right] \end{aligned} \tag{17}$$

Note that PLL provides the phase angle of the PCC voltage, and consequently determines the accuracy of the stator voltage

This article has been accepted for publication in a future issue of this journal, but has not been fully edited. Content may change prior to final publication. Citation information: DOI 10.1109/JESTPE.2019.2901747, IEEE Journal of Emerging and Selected Topics in Power Electronics

oriented vector control. Hence, the impedance behavior of DFIG can be influenced by the PLL dynamics. The second term in (17) reflects the impact of PLL.

The effects of PLL are most pronounced around the fundamental frequency in the range that corresponds to the bandwidth of the PLL [33]. It indicates that the higher the bandwidth of PLL, the more significant it will effect the impedance and the wider the frequency range it will affect. However, the bandwidth of PLL is rarely set to a high value for the sake of stability. That means neglecting the PLL dynamics is relatively reasonable for SSO analysis when the bandwidth of PLL is not large, and thus the impedance model of DFIG can be simplified as:

$$Z_{\mathrm{dfig}}(s)=\frac{r_{\mathrm{r}}+H_{\mathrm{r}}(s-j\omega_1)-jK_{\mathrm{dr}}}{S_{\mathrm{lip}}(s)}+sL_{\mathrm{r}}+r_{\mathrm{s}}+sL_{\mathrm{s}} \tag{18}$$

B. Impedance Model of WFVSC

The control structure of WFVSC station is depicted in Fig. 1. The control of both WFVSC and grid-side VSC (GSVSC) include two cascade control loops. The outer control loops are associated with the voltage controls, while the inner control loops are current controls. WFVSC regulates the ac voltage and supplies the sinusoidal voltage to the PCC. GSVSC regulates the dc voltage on the HVDC-link and the reactive power. Since this paper focuses on the interaction between DFIG and WFVSC, the detailed modeling will be represented only for WFVSC. The control of WFVSC are based on dq reference frame, in which the d-axis is orientated to the grid voltage v_{o} and q-axis leading the d-axis by 90°.

The dynamic equations of the converter in abc frame can be expressed as:

$$v_{\mathrm{o}}=v_{\mathrm{c}}-Z_{\mathrm{c}}i_{\mathrm{c}}=v_{\mathrm{c}}-sL_{\mathrm{f}}i_{\mathrm{c}}-j\omega_1L_{\mathrm{f}}i_{\mathrm{c}} \tag{19}$$

where Z_{c} is the filter impedance of the converter. Note that L_{f} instead of C_{f} dominates in the subsynchronous frequency region.

The reference current to current controller and the reference voltage to determine the output voltage of the converter can be defined by:

$$\begin{cases} i_{\mathrm{cdref}}=H_{\mathrm{v}}(s)(v_{\mathrm{odref}}-v_{\mathrm{od}}) \\ i_{\mathrm{cqref}}=H_{\mathrm{v}}(s)(v_{\mathrm{oqref}}-v_{\mathrm{oq}}) \end{cases} \tag{20}$$

$$\begin{cases} v_{\mathrm{cd}}=H_{\mathrm{c}}(s)(i_{\mathrm{cdref}}-i_{\mathrm{cd}})+v_{\mathrm{od}}-\omega_1L_{\mathrm{f}}i_{\mathrm{cq}} \\ v_{\mathrm{cq}}=H_{\mathrm{c}}(s)(i_{\mathrm{cqref}}-i_{\mathrm{cq}})+v_{\mathrm{oq}}+\omega_1L_{\mathrm{f}}i_{\mathrm{cd}} \end{cases} \tag{21}$$

The modeling of the system circuit and the control topology are based on abc and dq frame respectively. Therefore, the transformation of (20) and (21) to abc frame is required in order to establish a linkage:

$$\begin{cases} i_{\mathrm{cref}}=H_{\mathrm{v}}(s-j\omega_1)(v_{\mathrm{oref}}-v_{\mathrm{o}}) \\ v_{\mathrm{c}}=H_{\mathrm{c}}(s-j\omega_1)(i_{\mathrm{cref}}-i_{\mathrm{c}})+v_{\mathrm{o}}+j\omega_1L_{\mathrm{f}}i_{\mathrm{c}} \end{cases} \tag{22}$$

To obtain the impedance of WFVSC in the frequency domain, the dynamic equations including v_{o} and i_{c} should be found by substituting (22) to (19):

$$v_{\mathrm{o}}=-\frac{H_{\mathrm{c}}(s-j\omega_1)+Z_{\mathrm{c}}}{H_{\mathrm{c}}(s-j\omega_1)H_{\mathrm{v}}(s-j\omega_1)}i_{\mathrm{c}}+v_{\mathrm{oref}} \tag{23}$$

By linearizing (23), the impedance model of WFVSC can be found as (24) without considering the dc dynamics when the system is stable. And (24) can be further represented as the sum of two terms:

$$\begin{aligned} Z_{\mathrm{vsc}}(s)&=-\frac{\Delta v_{\mathrm{o}}}{\Delta i_{\mathrm{c}}}=\frac{H_{\mathrm{c}}(s-j\omega_1)+Z_{\mathrm{c}}}{H_{\mathrm{c}}(s-j\omega_1)H_{\mathrm{v}}(s-j\omega_1)} \\ &=\frac{1}{H_{\mathrm{v}}(s-j\omega_1)}+\frac{Z_{\mathrm{c}}}{H_{\mathrm{c}}(s-j\omega_1)H_{\mathrm{v}}(s-j\omega_1)} \end{aligned} \tag{24}$$

C. Simplified Equivalent Circuit of the Whole System

To investigate the mechanism and the characteristics of SSO phenomenon between DFIG-based wind farm and VSC-HVDC system, the impedance model of the whole system should be established by aggregating the impedance models of DFIG, WFVSC and transmission line on the PCC.

The impedance models of DFIG both with and without PLL have been built in Section III-A. Thus, the verification and comparison of the impedance models are performed. The positive sequence impedance of DFIG is measured from 0 ~ 100 Hz with 30 points in Fig. 8 using the method of injecting current. The operating condition for measurement is that the wind speed is set to 7.5 m/s and $K_{\mathrm{ppll}}=60$ pu, while the other parameters are given in the Appendix.

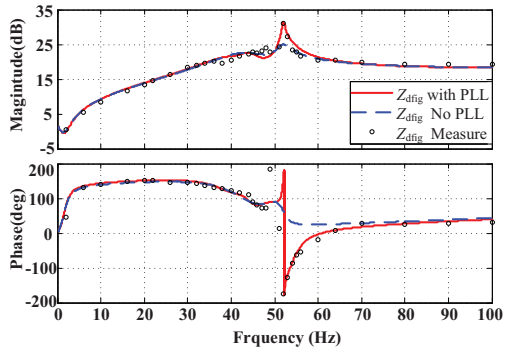

Fig. 8. Comparison of the impedance models of DFIG and the measurement results.

It is obvious that the responses predicted by the analytical models in (17) and (18) match the scanned impedance response well especially in the subsynchronous frequency region. In addition, the analytical model in (17) is more accurate than the model in (18) especially in the phase frequency curve due to the consideration of PLL. The second term in (17) demonstrates the influence of PLL on the DFIG impedance. This term equals to 1 when the PLL unit is not considered, and then (17) and (18) take the same form. It can be concluded that the model in (17) is suitable to analyse the influence of PLL parameters on SSO. However, it is much more complex than the model in (18). Note that the model in (18) can also be applied to the SSO analysis, when the bandwidth of PLL is not large enough and the influence of PLL is not remarkable. Thus, in order to simplify the analysis of the impact of factors including number of DFIGs, wind speed, and converter controller parameters on the SSO characteristics, the model in (18) is adopted to build the simplified equivalent circuit of the whole system. In contrast, the model in (17) is applied to analyze the influence of PLL parameters separately.

This article has been accepted for publication in a future issue of this journal, but has not been fully edited. Content may change prior to final publication. Citation information: DOI 10.1109/JESTPE.2019.2901747, IEEE Journal of Emerging and Selected Topics in Power Electronics

Noticeably, the influence of delays is not considered in this paper because the bandwidth of the PLL loop is normally not large [31], [32], while the effect of the delays is usually represented in high frequency range [22], [25]. And this assumption aligns with the measurement results in Fig. 8.

To intuitively analyze the factors that have great impact on SSO, an impedance-based simplified equivalent circuit of the whole system is established with some simplifications as follows,

- ΔV_{s1}, ΔV_{s2} are disturbances in output voltage of RSC and WFVSC which can be ignored in stable state.
- K_{pr} is dominant in the RSC current control loop while K_{ir} and K_{dr} is less important, as shown in Fig. 9(a).
- $1/H_v(s)$ exerts most powerful impact on the impedance of WFVSC while the influence of $Z_c/(H_c(s)H_v(s))$ is subordinated, as shown in Fig. 9(b).

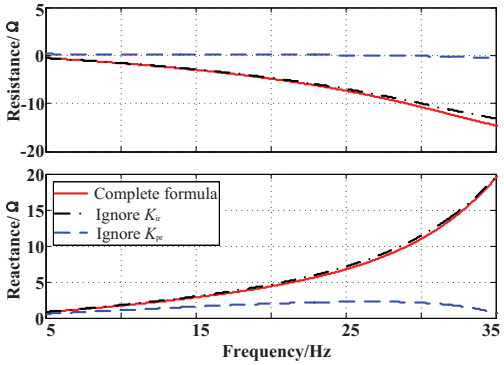

(a)

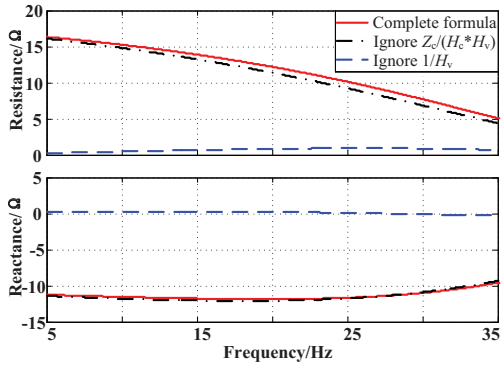

(b)

Fig. 9. The impedance-frequency curves of: (a) DFIG, (b) WFVSC.

Fig. 9(a) illustrates the comparative analysis of the impact of K_{pr} and K_{ir} on the impedance of DFIG. The parameters are listed in Appendix. The result shows that the influence of K_{pr} is much larger than K_{ir}. Therefore, only the proportional gain of PI controller will be analysed in this paper. Fig. 9(b) demonstrates the comparative analysis of the impact of $1/H_v(s)$ and $Z_c/(H_c(s)H_v(s))$ on the impedance of WFVSC under the same condition. The result shows that the influence of $1/H_v(s)$ is much larger than $Z_c/(H_c(s)H_v(s))$ because the magnitude of Z_c is small at subsynchronous frequency region. As discussed above, the simplified equivalent circuit of the whole system which considers the multiple DFIGs is derived for the convenient analysis of the SSO characteristics.

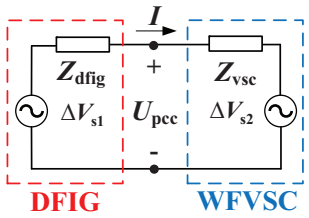

Fig. 10. Impedance based equivalent model of the whole system.

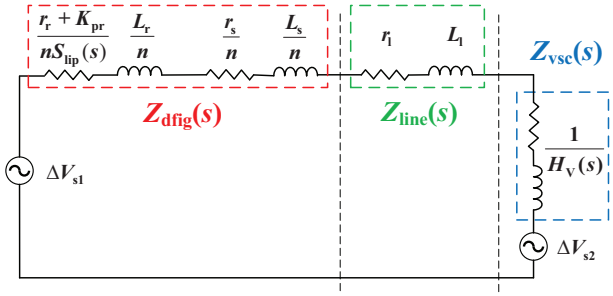

Fig. 11. Simplified equivalent circuit of the whole system.

As shown in Fig. 10, the impedance-based equivalent model of the whole system is composed of the impedance models of DFIG and WFVSC on PCC. In order to simplify the analysis of the impact factors which have great impact on SSO characteristics, the simplified models of DFIG and WFVSC are adopted according to the above discussion. And then the resistance and reactance of the whole system can be further represented by the sum of each part as shown in Fig. 11, where $Z_{line} = r_l + sL_l$ is the equivalent impedance of the transmission line and the transformers. The circuit parameters in the simplified equivalent model can intuitively reflect the impact of various factors including the number of DFIGs, wind speed and controller parameters of DFIG or WFVSC.

IV. Mechanism and Characteristics Analysis of SSO

The stability criterion of SSO is represented based on RLC series resonance circuit firstly. Then the factors which have great impact on the characteristics of SSO are analyzed. Moreover, the effect of PLL parameters on SSO is analyzed based on the impedance model of DFIG with the PLL unit.

A. SSO Stability Criterion Based on Second-Order RLC Series Resonance Circuit

In order to assess the SSO stability of the system, the simplified equivalent circuit of the whole system can be further represented by the equivalent second-order RLC series resonance circuit. Therefore, the SSO stability criterion of the whole system can be derived from the resonant principle as:

$$\begin{cases} R_{sys} = \mathrm{Re}(Z_{dfig}(s) + Z_{line}(s) + Z_{vsc}(s)) > 0 \\ X_{sys} = \mathrm{Im}(Z_{dfig}(s) + Z_{line}(s) + Z_{vsc}(s)) = 0 \end{cases} \tag{25}$$

where R_{sys} and X_{sys} are the resistance and reactance of the whole system, respectively. The self-excitation of the equivalent circuit will occur at the resonant frequency while $X_{sys} = 0$. And if $R_{sys} > 0$, the damping of the equivalent circuit is positive, which indicates that the system is stable; otherwise,

This article has been accepted for publication in a future issue of this journal, but has not been fully edited. Content may change prior to final publication. Citation information: DOI 10.1109/JESTPE.2019.2901747, IEEE Journal of Emerging and Selected Topics in Power Electronics

the diverging electrical oscillation tends to appear at the resonant frequency. Therefore, the start-oscillating condition is directly determined by R_{sys} and X_{sys}, which means both DFIG and WFVSC have impact on the oscillation.

In order to apply the criterion to the stability analysis of the system, Scenario 1 in Section II-B is considered as an example. Under the same condition as Scenario 1, the impedances of DFIGs and WFVSC at subsynchronous frequency regions are measured using the injecting current method. The small-signal current perturbation is injected to the PCC and the resulting response in voltage is measured, which resembles the mathematical process of harmonic linearization. The DFT is adopted to analyze the different harmonic voltage and current at each frequency to calculate the impedance. The impedance-frequency curves of the whole system can be obtained according to (25).

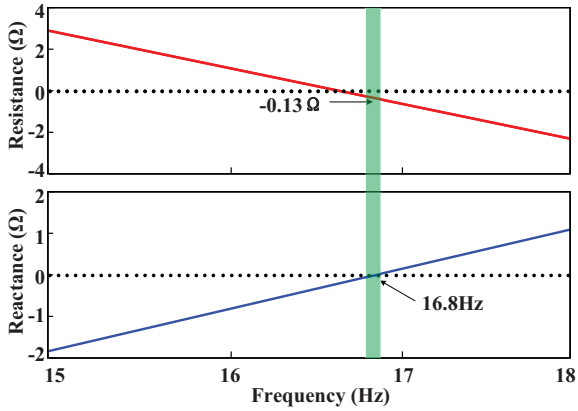

Fig. 12. The impedance-frequency curves of the system under condition of Scenario 1.

The mechanism of SSO is explained as follows. As shown in Fig. 12, the oscillating frequency of the system is determined by the zero-crossing frequency in the reactance-frequency curve (16.8 Hz). And the corresponding value in the resistance-frequency curve at the oscillating frequency is -0.13 Ω which means the resistance of the whole system is negative. In combination with Fig. 9, it is obvious that DFIGs behave as an inductance in series with a negative resistance at resonance point, whose interaction with WFVSC (represents as a positive resistance-capacitance) constitutes the equivalent resonance circuit. Since the negative resistance generated by DFIGs overcomes the positive resistance of WFVSC and line, the resistance of the equivalent resonance circuit is negative at resonance point, which means the SSO phenomenon tends to appear for the negative damping effect of the system. More operating condition

The error of oscillating frequency measured in Fig. 12 is slight compared with the value obtained from the spectrum analysis in Fig. 4 (17.1 Hz). Generally speaking, within the tolerance range, the results of two methods are in good agreement with each other, which indicates that the SSO stability criterion based on the equivalent resonance circuit is effective. The reason lead to the error is that the mathematical process of harmonic linearization is not completely accurate. Besides, this criterion will be applied and validated in Section V under different operation conditions according to the variation of number of DFIGs, wind speed and converter controller parameters.

B. Number of Grid-Connected DFIGs

According to the simplified equivalent circuit depicted in Fig. 11, the resistance and reactance of DFIGs, WFVSC and the whole system can be represented as (26). Evidently, the number of grid-connected DFIGs has directly impact on the equivalent impedance of rotor and stator.

$$\begin{cases} R_{sys} = \underbrace{\dfrac{r_r + K_{pr}}{nS_{lip}} + \dfrac{r_s}{n}}_{R_{dfig}} + r_1 + \underbrace{\dfrac{K_{pv}(\omega_1-\omega)^2}{K_{pv}^2(\omega_1-\omega)^2 + K_{iv}^2}}_{R_{vsc}} \\ X_{sys} = \underbrace{\dfrac{\omega(L_r+L_s)}{n}}_{X_{dfig}} + \omega L_1 - \underbrace{\dfrac{K_{iv}(\omega_1-\omega)}{K_{pv}^2(\omega_1-\omega)^2 + K_{iv}^2}}_{X_{vsc}} \end{cases} \tag{26}$$

In order to analyse the impact of the number of grid-connected DFIGs (n) on SSO, the impedance-frequency curves of DFIGs, WFVSC and the whole system are depicted according to (26). As shown in Fig. 13, the curves denoted with '1' corresponding to the operating condition of Case 1 in Section II-B with $n = 100$ while the curves denoted with '2' corresponding to the same operating condition with $n = 120$. Without loss of generality, the analysis of different n is similar when other parameters of the system remain the same. Therefore, the influence of 20% increase of n is analysed as an example. Notably, the upper limit of n is restricted by the capacity of VSC-HVDC system.

According to (26), with n increasing from 100 to 120, both the equivalent reactance and resistance of DFIGs decrease with an inverse proportional trend (the resistance becomes positively larger). The corresponding influence to the impedance curves in Fig. 13 is represented as follows: both the reactance-frequency curves of DFIGs and the whole system, X_{dfig1} and X_{sys1}, are shifted downward to X_{dfig2} and X_{sys2}. The zero-crossing frequency in X_{sys1} and X_{sys2} are defined as f_1 and f_2 respectively, and the resonant frequency of the system is increased from f_1 to f_2. Both the resistance-frequency curves of DFIGs and the whole system, R_{dfig1} and R_{sys1}, are shifted upward to R_{dfig2} and R_{sys2}. As shown in Fig. 13, the corresponding resistance in R_{sys1} at f_1 is defined as R_1 while the corresponding resistance in R_{sys2} at f_2 is defined as R_2. Obviously, there is $R_1 > 0 > R_2$, which means the equivalent resistance of the system changes from positive to negative. Hence, the SSO damping decreases with the increase of n while the oscillating frequency increases at the same time.

The fundamental reason is that the downtrends of R_{dfig} is fast at subsynchronous frequency region. Since R_{dfig} and X_{dfig} are the inverse proportional functions of n, the impact of n on the impedance and oscillating frequency of the system is significant when n is not large. However, this impact will be weakened with n increases.

C. Wind speed

The rotor speed is directly determined by the wind speed when DFIGs run under MPPT mode. Hence, the analysis of

This article has been accepted for publication in a future issue of this journal, but has not been fully edited. Content may change prior to final publication. Citation information: DOI 10.1109/JESTPE.2019.2901747, IEEE Journal of Emerging and Selected Topics in Power Electronics

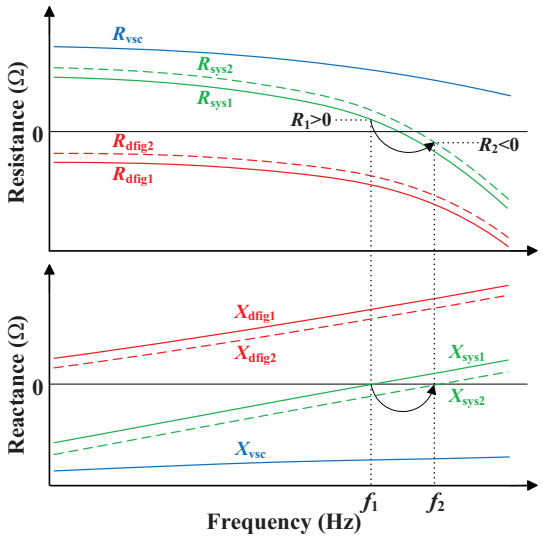

Fig. 13. Impact of the number of grid-connected DFIGs on the impedance-frequency curves.

the wind speed can be equivalently replaced by the rotor speed. According to (26), the equivalent negative resistance of DFIGs is mainly contributed by the rotor since $S_{\text{lip}} = (s - j\omega_{\text{r}})/s < 0$ under subsynchronous speed. Furthermore, the lower the rotor speed is, the more negative the slip is. In other words, the absolute value of $(r_{\text{r}} + K_{\text{pr}})/nS_{\text{lip}}$ is larger when the wind speed is low, which means DFIGs will provide more negative damping for the whole system. Therefore, the decrease of the wind speed will increase the risk of SSO.

D. RSC Current Loop Gain K_{pr}

According to (26), the equivalent resistance of DFIGs can be expressed as $(r_{\text{r}} + K_{\text{pr}})/nS_{\text{lip}} + r_{\text{s}}/n$. The proportional gain K_{pr} of RSC current controller has directly impact on the resistance of the rotor. And the resistance of DFIGs will become negative when K_{pr} is set to a relatively large value in order to achieve the requirement of the response speed and tracking accuracy. Furthermore, the larger K_{pr} results in much more negative resistance of DFIGs which reduces the equivalent damping and makes the system more vulnerable to SSO.

E. WFVSC Voltage Loop Gain K_{pv}

In order to analyse the impact of the proportional gain K_{pv} in voltage controller of WFVSC, the impedance-frequency curves of DFIGs, WFVSC and the whole system are depicted according to (26). As shown in Fig. 14, the curves denoted with '1' corresponding to the operating condition of case1 in Section II-B with $K_{\text{pv}} = 2.0$ pu while the curves denoted with '2' corresponding to the same operating condition with $K_{\text{pv}} = 2.2$ pu. Without loss of generality, the analysis process of the different K_{pv} is similar when other parameters of the system remain the same. Therefore, the influence of the 10% increase of K_{pv} is analysed as an example. Notably, the upper limit and lower limit of K_{pv} are restricted by the cost of devices and the demand of response speed respectively.

According to (26), with K_{pv} increasing from 2.0 to 2.2 pu, the equivalent reactance of WFVSC follows a parabolic trend increase while the equivalent resistance of WFVSC decreases with an inverse proportional trend. The corresponding influence to the impedance curves in Fig. 14 is represented as follows: both the reactance-frequency curves of WFVSC and the whole system, X_{vsc1} and X_{sys1}, are shifted upward to X_{vsc2} and X_{sys2}; The zero-crossing frequency in X_{sys1} and X_{sys2} are defined as f_1 and f_2 respectively, and the resonant frequency of the system is reduced from f_1 to f_2; Both the resistance-frequency curves of WFVSC and the whole system, R_{vsc1} and R_{sys1}, are shifted downward to R_{vsc2} and R_{sys2}. As shown in Fig. 14, the corresponding resistance in R_{sys1} at f_1 is defined as R_1 while the corresponding resistance in R_{sys2} at f_2 is defined as R_2. Obviously, there is $R_1 < 0 < R_2$, which means the equivalent resistance of the system changes from negative to positive. Hence, the SSO damping increases with the increase of K_{pv} while the oscillating frequency decreases at the same time.

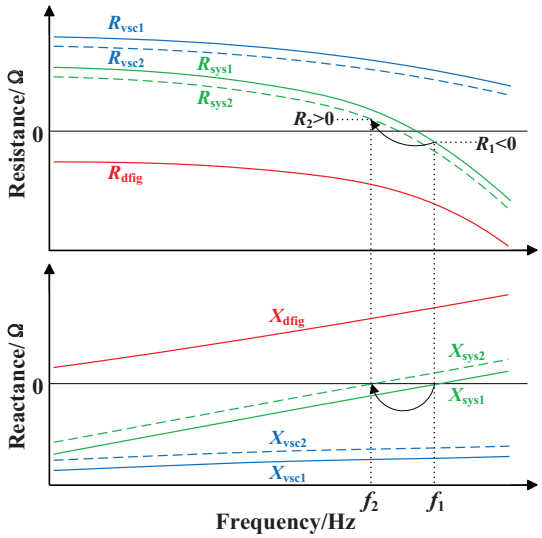

Fig. 14. Impact of K_{pv} on the impedance-frequency curves.

F. WFVSC Current Loop Gain K_{pc}

According to the analysis in Section III-C, $Z_{\text{c}}/(H_{\text{c}}(s)H_{\text{v}}(s))$ is neglected when focusing on the influence of K_{pv}. However, in order to analyze the impact of WFVSC current loop gain K_{pc} on the SSO characteristics, this term is reconsidered here while with K_{iv} neglected.

$$\frac{Z_{\text{c}}}{H_{\text{c}}(s)H_{\text{v}}(s)} = \frac{\omega X_{\text{c}}}{\omega_1 K_{\text{pv}}}\left(\frac{K_{\text{ic}}(\omega_1-\omega)}{K_{\text{pc}}^2(\omega_1-\omega)^2+K_{\text{ic}}^2} + \frac{jK_{\text{pc}}(\omega_1-\omega)^2}{K_{\text{pc}}^2(\omega_1-\omega)^2+K_{\text{ic}}^2}\right) \tag{27}$$

According to (27), the influence of this term is equivalent to inserting a positive resistance in series with an inductance to the impedance model of WFVSC. Similar to the analysis in Fig. 14, when K_{pc} increases near the critical point of oscillation, the equivalent inserted reactance follows a parabolic trend increase which leads to a rise in the reactance-frequency curves of WFVSC and the whole system. Correspondingly, the resonant frequency of the system is reduced and the decrease of the positive resistance of WFVSC and the whole system

This article has been accepted for publication in a future issue of this journal, but has not been fully edited. Content may change prior to final publication. Citation information: DOI 10.1109/JESTPE.2019.2901747, IEEE Journal of Emerging and Selected Topics in Power Electronics

is offset. Therefore, the system damping is enhanced with the increase of K_{pc} while the oscillating frequency decreases at the same time.

G. PLL Control Gain K_{ppll}

The effect of PLL dynamics on the SSO analysis is not yet considered in the above parts. In this part, the influence of PLL parameters on the SSO characteristics is studied based on the impedance model in (17) which takes the PLL dynamics into consideration.

According to (17), the influence of PLL mainly reflects on the term $(i_{rd}H_r(s-j\omega_1)/S_{lip}(s)+U_{rd})T_{pll}(s-j\omega_1)$ which is too complex to simplify and analyse directly. Therefore, the impedance-frequency curves of DFIG in the subsynchronous frequency region are depicted in Fig. 15 to help the analysis of the impedance-frequency characteristics of DFIG with different bandwidths of PLL.

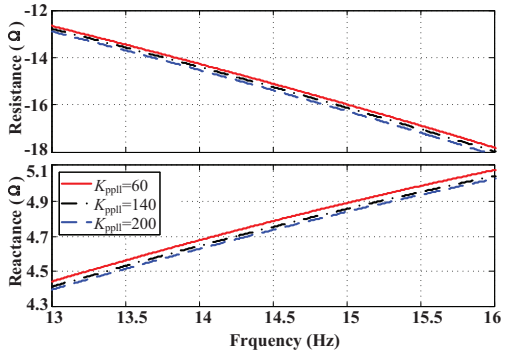

Fig. 15. The impedance-frequency curves of DFIG with different PLL controller gain K_{ppll}.

Note that when the bandwidth of PLL increases with K_{ppll} from 60 to 200 pu, the equivalent resistance of DFIG becomes more negative while the reactance is slightly reduced. By combining Fig. 14, this trend of the change means the oscillating frequency of the system increases and the equivalent resistance of the system becomes more negative. It can be concluded that the wider the bandwidth of PLL, the more significant its negative effects on the system damping and the system stability. In other words, though the larger K_{ppll} results in the faster response speed of the converter control, SSO is more likely to happen due to the increased negative real part of DFIG output impedance. Therefore, the parameters of PLL is important in the study of SSO between DFIGs and VSC system.

V. Simulation Verification

The time-domain simulations are conducted two-fold. First, the number of the DFIGs and the wind speed are analyzed. On the other hand, the impact factors of the control parameters are also investigated. The comparisons with analytical models in the previous sections are presented.

A. Number of Grid-Connected DFIGs and Wind Speed

As shown in Fig. 16, the equivalent resistance and the oscillating frequency of the whole system are measured under the operating condition. The number of grid-connected DFIGs ranges from 60 to 180 and the wind speed ranges from 7.5 to 9.5 m/s, while other system parameters keep unchanged. From the simulation results, it can be observed that the higher the wind speed, the more positive the system resistance. The higher the oscillating frequency means both the system stability and the oscillating frequency have the positive correlation with the wind speed. In addition, when the number of grid-connected DFIGs increases under the fixed wind speed, the system resistance decreases while the oscillating frequency increases, which means the system stability has a negative correlation with n while the oscillating frequency has a positive correlation with n. It can be concluded that SSO usually happens under a lot numbers of DFIG-WTs connected with low wind speed.

Fig. 17 shows the output active power responses to the sudden change of the load at t=15 s under the different operating conditions. As shown in Fig. 17(a), the critical wind speed for SSO is 8.5 m/s on condition that the number of grid-connected DFIGs is set to 100. When the wind speed is higher than 8.5 m/s, SSO is divergent. Otherwise, SSO is convergent. As shown in Fig. 17(b), SSO is intensified while the number of grid-connected DFIGs increases from 100 to 120. Therefore, the simulation results align with the analysis in Section IV-B and Section IV-C.

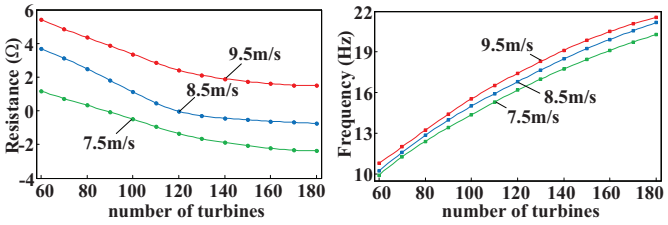

(a) (b)

Fig. 16. Impact of the number of grid-connected DFIGs under three different wind speeds on the: (a) resistance, (b) oscillating frequency.

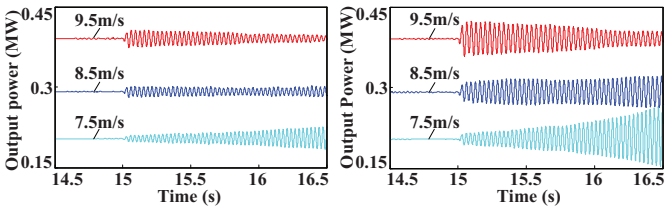

(a) (b)

Fig. 17. The output power varies with the number of grid-connected DFIGs under three different wind speeds: (a) 100 turbines, (b) 120 turbines.

B. The Proportional Gains of PI Controllers

The impact of K_{pr}, K_{pv}, K_{pc} and K_{ppll} on SSO characteristics is analysed in this part under the following operating condition: the number of DFIGs is set to 100, the wind speed is set to 7.5 m/s, and other system parameters keep unchanged. And the simulation results show the output active power responses of wind farms for a sudden change of the load at t=15 s.

As shown in Fig. 18(a), the equivalent resistance and the oscillating frequency of the whole system are measured with

This article has been accepted for publication in a future issue of this journal, but has not been fully edited. Content may change prior to final publication. Citation information: DOI 10.1109/JESTPE.2019.2901747, IEEE Journal of Emerging and Selected Topics in Power Electronics

K_{pr} in the range of 0.1 to 0.6 pu. It can be observed that the larger the gain K_{pr}, the more negative the system resistance is, and the lower the oscillating frequency will be, which means both the system stability and the oscillating frequency have a negative correlation with K_{pr}. It can be concluded that SSO usually happens when K_{pr} is large. As shown in Fig. 19(a), the critical value of K_{pr} for SSO is about 0.6 pu. When K_{pr} increases from 0.1 to 0.6 pu, the convergence speed of SSO becomes slower gradually and the oscillation state finally changes from convergent to invariable. Therefore, the simulation results align with the analysis in Section IV-D.

As shown in Fig. 18(b), K_{pv} changes from 1.7 to 2.3 pu in the measurements of the equivalent resistance and the oscillating frequency of the system. As can be seen, the system stability has a positive correlation with K_{pv} while the oscillating frequency has a negative correlation with K_{pv}, which means SSO usually happens when K_{pv} is small. As shown in Fig. 19(b), the critical value of K_{pv} for SSO is about 2.0 pu, and the oscillation state changes from divergent to convergent when K_{pv} increases from 1.8 to 2.2 pu. In addition, the SSO characteristics is affected more by K_{pv} than by K_{pr} according to the waveforms in Fig. 19(a) and Fig. 19(b). Therefore, the simulation results align with the analysis in Section IV-E.

Fig. 18(c) illustrates the result of measurements when K_{pc} changes from 0.44 to 0.56 pu. It can be observed that the system stability has a positive correlation with K_{pc} while the oscillating frequency has a negative correlation with K_{pc}, which means SSO usually happens when K_{pc} is small. According to Fig. 19(c), the critical value of K_{pc} for SSO is about 0.50 pu, and the oscillation state changes from divergent to convergent When K_{pc} increases from 0.46 to 0.54 pu. However, by comparing the waveforms in Fig. 19(b) and Fig. 19(c), it can be found that K_{pc} has less impact on the SSO characteristics than K_{pv}. This conclusion agrees with the analysis in Section IV-F.

Fig. 18(d) shows the result of measurements when K_{ppll} changes from 20 to 220 pu. As can be seen, the system stability has a negative correlation with K_{ppll} while the oscillating frequency has a positive correlation with K_{ppll}. According to Fig. 19(d), the critical value of K_{ppll} for SSO is about 60 pu. When K_{ppll} increases from 60 to 200 pu, the divergence speed of SSO becomes faster gradually and the oscillation state finally changes from invariable to divergent. By comparing the waveforms in Fig. 19(c) and Fig. 19(d), it can be found that the influence of the PLL dynamics is not as large as the current loop, but it should not be ignored for SSO analysis especially when the bandwidth of PLL is large. This conclusion agrees with the analysis in Section IV-G.

VI. Experimental Results

To further verify the impedance model and the simulation results, a dSPACE based hardware-in-loop (HIL) experiment is carried out. The hardware platform of HIL experiment is shown in Fig. 20. The main system is simulated in the DS1006 board where the controller is implemented on another dSPACE platform (DS1104 board). The DS1104 board is equipped

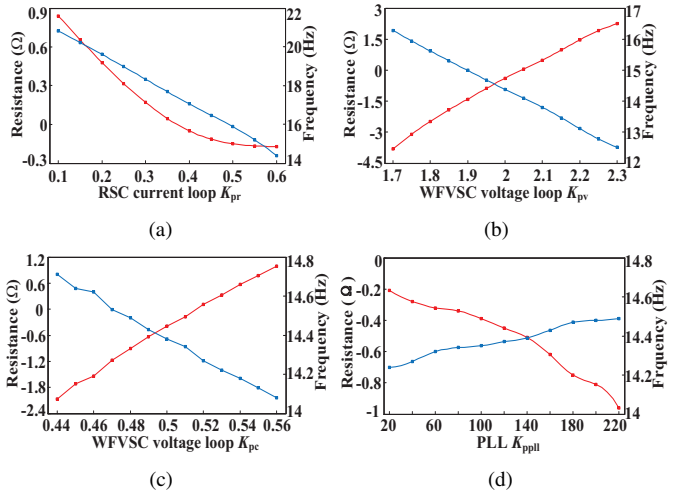

Fig. 18. Impact of the controller parameters on the system resistance and the oscillating frequency: (a) K_{pr}. (b) K_{pv}. (c) K_{pc}. (d) K_{ppll}. (red curve denotes the system resistance and blue curve denotes the oscillating frequency)

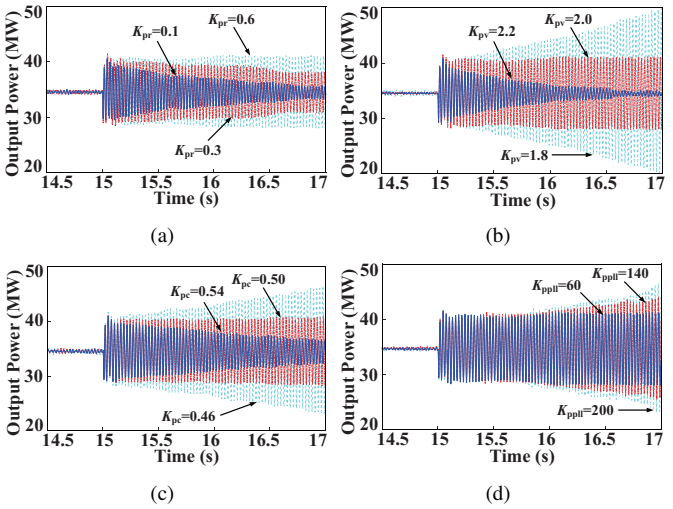

Fig. 19. The output power varies with the controller parameters: (a) K_{pr}. (b) K_{pv}. (c) K_{pc}. (d) K_{ppll}.

with eight digital-to-analogue channels and eight analogue-to-digital channels to interface the measured signals to/from the control system. The software code is generated by the Real-Time WorkShop under a MATLAB/Simulink environment.

The advantages of HIL experiment compared with the simulation are mainly as follows: there exist uncertain measurement disturbances in the HIL experiment which cannot be accurately considered in the simulation; the HIL experiment results respond slightly slower than that of simulation results since the existence of time delay of the real-time controller; Some unknown harmonics may occur in the HIL experiment caused by the capacitors or inductors between the signal transmission cables and the dSPACE device.

The impedance measurement system shown in Fig. 21 uses the DS1006 board to inject the current perturbation. The range of impedance measurements in the experiment is 0 $\sim$ 100 Hz with 20 measurement points. The parameters used in the experiments are the same with the measurement in Fig. 8. The experimental results of the sequence impedance measurement for DFIG and WFVSC are shown in Fig. 21. It is evident that

This article has been accepted for publication in a future issue of this journal, but has not been fully edited. Content may change prior to final publication. Citation information: DOI 10.1109/JESTPE.2019.2901747, IEEE Journal of Emerging and Selected Topics in Power Electronics

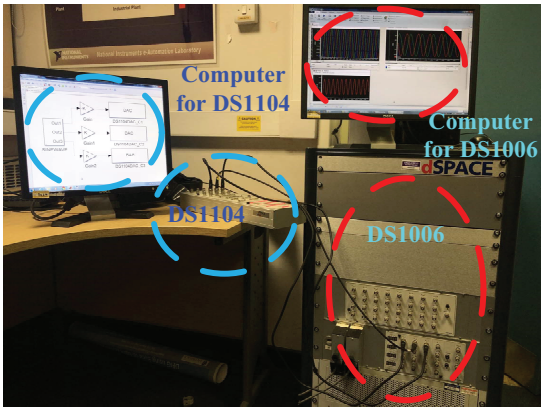

Fig. 20. The hardware platform of HIL experiment.

the experimental measurement results show good agreement with the built impedance model, thus the sequence impedance models of DFIG and WFVSC are validated.

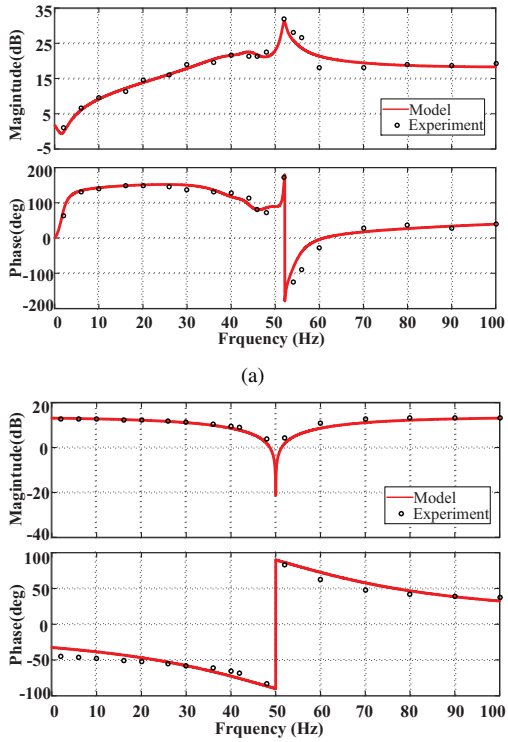

(a)

(b)

Fig. 21. Measurement results compared with model: (a) Impedance of DFIG, (b) Impedance of WFVSC.

Then the simulation results are also validated. The parameters used in the experiments are the same with the simulation analysis. The terminal d-axis current and 3-phase current of DFIG with the change of the number of DFIG-WTs, K_{ppll}, and K_{pv} are obtained from the real-time simulation of the system on the DS1006 board. Fig. 22 shows these current dynamics after a load disturbance at t = 15 s with the number of DFIG-WTs are 100 and 120, respectively. It is clear that the three phase current is distorted and the d-axis current becomes divergent with the increase of the number of DFIG-WTs. Figure 23 shows the current dynamics with the increase of K_{pv}. In Fig. 23(a), the current is unstable with K_{pv} = 1.8 pu, which agrees with the simulation results in Fig. 19(b). When increasing K_{pv} to 2.2 pu, the current becomes convergent as shown in Fig. 23(b). Besides, two sets of PLL parameters, such as K_{ppll} = 60 and 200 pu, are tested in Fig. 24. It is clear that the state of oscillation become worse when the K_{ppll} is increased, which closely correlate with the simulation results in Fig. 19(d). According to the above analysis, it can be concluded that the HIL experiment results and simulation results match each other well.

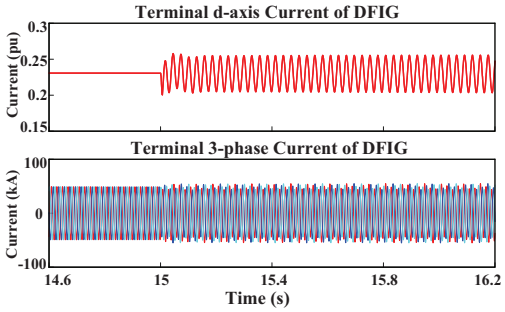

(a)

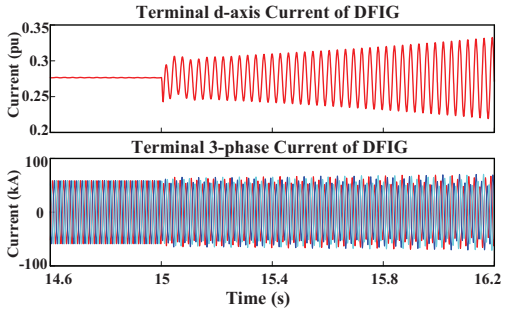

(b)

Fig. 22. Measured terminal d-axis current and 3-phase current of DFIG under different conditions: (a) number of DFIG-WTs is 100, (b) number of DFIG-WTs is 120.

VII. Conclusions

DFIG-based wind farm faces potential risk of SSO when connected to VSC-HVDC system. In this paper, the impedance models of DFIG with and without considering the PLL dynamics are both derived to help understand the mechanism and characteristics of SSO. Then the impedance-based simplified equivalent circuit of the system is proposed. On the basis of this model, reasonable mechanism explanation of SSO is revealed, and the impact factors of the SSO are further studied. In addition, the effect of PLL control parameters on SSO is also analyzed. It is revealed that the influence of the PLL dynamics can not be ignored for SSO analysis when the bandwidth of PLL is large.

As far as the operating conditions concerned, the risk of SSO of the system increases in low wind speed condition and when a limited number of DFIGs are connected. Regarding the controller parameters, the system stability has a positive correlation with K_{pv} and K_{pc}. And the system stability also has a negative correlation with K_{pr} and K_{ppll}. The mechanism of the influence of these factors on SSO is that the change of these parameters reshapes the total damping at the resonant frequency. And SSO may appear due to the negative damping under the undesired operating conditions and controller

This article has been accepted for publication in a future issue of this journal, but has not been fully edited. Content may change prior to final publication. Citation information: DOI 10.1109/JESTPE.2019.2901747, IEEE Journal of Emerging and Selected Topics in Power Electronics

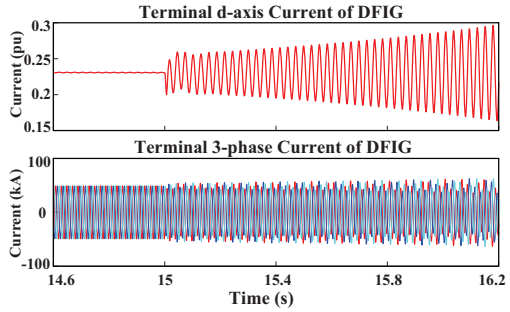

(a)

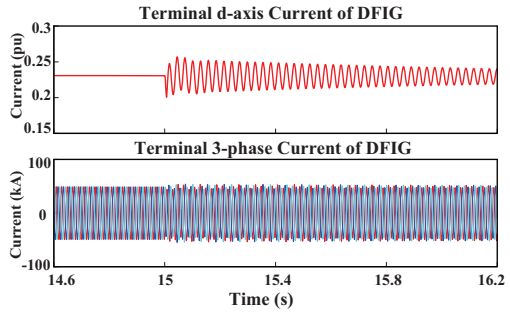

(b)

Fig. 23. Measured terminal d-axis current and 3-phase current of DFIG under different conditions: (a) K_{pv} = 1.8 pu, (b) K_{pv} = 2.2 pu.

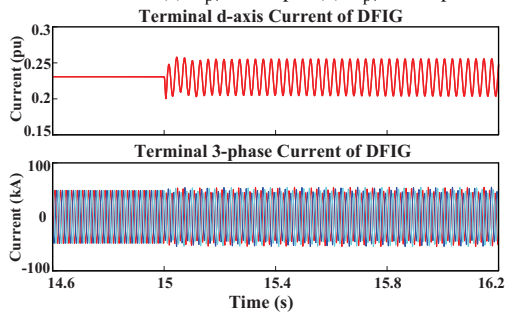

(a)

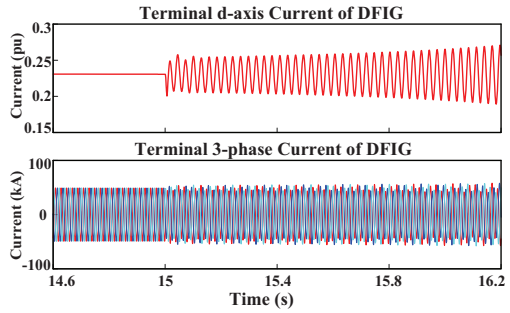

(b)

Fig. 24. Measured terminal d-axis current and 3-phase current of DFIG under different conditions: (a) K_{ppll} = 60 pu, (b) K_{ppll} = 200 pu.

parameters. All the theoretical analysis above are verified by both the time-domain simulation and HIL experiments with detailed models.

APPENDIX

TABLE I
THE PARAMETERS OF DFIG

Parameters	Value	Parameters	Value
Rated power	1.5 MW	r_s	0.0023 pu
Rated voltage	575 V	L_s	0.16 pu
Rated rotor speed	1.2 pu	r_r	0.0016 pu
Dc capacitor	0.01 F	L_r	0.18 pu
Dc voltage	1150 V	L_m	2.9 pu

TABLE II
THE PARAMETERS OF VSC-HVDC AND AC TRANSMISSION LINE

VSC Parameters	Value	Line Parameters	Value
VSC capacity	300 MW	Base MVA	100 MW
Dc capacitor	1250 μF	Line length	25 mile
Dc voltage	200 kV	Rated voltage	110 kV
L_f	8 mH	R_l	0.1855 Ω/mile
C_f	10 μF	L_l	1.685 mH/mile

REFERENCES

[1] N. Flourentzou, V. G. Agelidis, and G. D. Demetriades, "VSC-based HVDC power transmission systems: An overview," *IEEE Trans. Power Electron.*, vol. 24, no. 3, pp. 592-602, Feb. 2009.

[2] M. P. Bahrman and B. K. Johnson, "The ABCs of HVDC transmission technologies," *IEEE Power Energy Mag.*, vol. 5, no.2, pp. 32-44, Mar. 2007.

[3] J. Hu, H. Yuan, and X. Yuan, "Modeling of DFIG-based WTs for small-signal stability analysis in DVC timescale in power electronized power systems," *IEEE Trans. Energy Convers.*, vol. 32, no. 3, pp. 1151-1165, Sept. 2017.

[4] H. Liu and J. Sun, "Impedance-based stability analysis of VSC-based HVDC systems," in *Proc. IEEE Workshop Control Model. Power Electron.*, Salt Lake City, UT, USA, Oct. 2013, pp. 1-8.

[5] L. Shen, M. Barnes, R. Preece, J. V. Milanovic, K. Bell, and M. Belivanis, "The effect of VSC-HVDC control on AC system electromechanical oscillations and DC system dynamics," *IEEE Trans. Power Del.*, vol. 31, no. 3, pp. 1085-1095, Jun. 2016.

[6] J. Lyu, P. Dong, G. Shi, X. Cai, H. Rao, and J. Chen, "Subsynchronous oscillation of large DFIG-based wind farms integration through MMC-based HVDC," in *Proc. IEEE PowerTech Conf.*, Chengdu, China, Dec. 2014, pp. 2401-2408.

[7] J. Lyu, X. Cai, M. Amin, and M. Marta, "Sub-synchronous oscillation mechanism and its suppression in MMC-based HVDC connected wind farms," *IET Gener. Transm. Distrib.*, vol. 12, no. 4, pp. 1021-1029, Jan. 2018.

[8] X. Dong and X. Xie, "Influence of DFIG controller parameter on SSR under all operation areas," in *Proc. IEEE PowerTech Conf.*, Chengdu, China, Dec. 2014, pp. 2618-2622.

[9] Z. Miao, "Impedance-model-based SSR analysis for type 3 wind generator and series-compensated network," *IEEE Trans. Energy Convers.*, vol. 27, no. 4, pp. 984-991, Dec. 2012.

[10] H. Liu and X. Xie, "Quantitative SSR analysis of series-compensated DFIG-based wind farms using aggregated RLC circuit model," *IEEE Trans. Power Syst.*, vol. 32, no. 1, pp. 474-483, Jan. 2017.

[11] L. Wang, X. Xie, Q. Jiang, H. Liu, Y. Li, and H. Liu, "Investigation of SSR in practical DFIG-based wind farms connected to a series-compensated power system," *IEEE Trans. Power Syst.*, vol. 30, no. 5, pp. 2772-2779, Sept. 2015.

[12] W. Du, C. Chen and H. Wang, "Subsynchronous interactions induced by DFIGs in power systems without series compensated lines," *IEEE Trans. Sustain. Energy*, vol. 9, no. 3, pp. 1275-1284, July. 2018.

[13] M. Cespedes and J. Sun, "Impedance modelling and analysis of grid-connected voltage-source converters," *IEEE Trans. Power Electron.*, vol. 29, no. 3, pp. 1254-1261, Mar. 2014.

[14] H. Liu and J. Sun, "Voltage stability and control of offshore wind farms with AC collection and HVDC transmission," *IEEE J. Emerg. Sel. Topics Power Electron.*, vol. 2, no. 4, pp. 1181-1189, Dec. 2014.

[15] Y. Huang, X. Zhai, J. Hu, D. Liu, and C. Lin, "Modeling and stability analysis of VSC internal voltage in DC-link voltage control timescale," *IEEE J. Emerg. Sel. Topics Power Electron.*, vol. 6, no. 1, pp. 16-28, Mar. 2018.

[16] M. Amin and M. Marta, "Understanding the origin of oscillatory phenomena observed between wind farms and HVDC systems," *IEEE J. Emerg. Sel. Topics Power Electron.*, vol. 5, no. 1, pp. 378-392, Mar. 2017.

[17] M. Amin and J. Lyu, "Oscillatory phenomena between wind farms and HVDC systems: The impact of control," in *Proc. IEEE Workshop*

Control Model. Power Electron., Vancouver, BC, Canda, Sept. 2015, pp. 1-8.

[18] L. Wang, Z. Yang, X. Lu, and A. V. Prokhorov, "Stability analysis of a hybrid multi-infeed HVDC system connected between two offshore wind farms and two power grids," *IEEE Trans. Ind. Appl.*, vol. 53, no. 3, pp. 1824-1833, May. 2017.

[19] L. P. Kunjumuhammed, B. C. Pal, C. Oates, and K. J. Dyke, "Electrical oscillations in wind farm systems analysis and insight based on detailed modeling," *IEEE Trans. Sustain. Energy*, vol. 7, no. 1, pp. 51-61, Jan. 2016.

[20] M. Cheah-Mane, L. Sainz, J. Liang, N. Jenkins, and C. E. Ugalde-Loo, "Criterion for the electrical resonance stability of offshore wind power plants connected through HVDC links," *IEEE Trans. Power Syst.*, vol. 32, no. 6, pp. 4579-4589, Nov. 2017.

[21] N. Cao, K. Chong, L. Qi, D. Jin, and Z. Song, "Impedance-based analysis on subsynchronous oscillation mechanism caused of VSC-HVDC with double-fed induction generator," *Chinese Automation Congress*, Jinan, China, Oct. 2017, pp. 3602-3608.

[22] X. Wang, L. Harnefors, and F. Blaabjerg, "A unified impedance model of voltage-source converter with PLL effect," *IEEE Trans. Power Electron.*, vol. 33, no. 2, pp. 1775-1787, Feb. 2018

[23] S. Zhou, X. Zou, and X. Yuan, "An improved design of current controller for LCL-type grid-connected converter to reduce negative effect of PLL in weak grid," *IEEE J. Emerg. Sel. Topics Power Electron.*, vol. 6, no. 2, pp. 648-663, Jan. 2018.

[24] B. Wen, D. Boroyevich, R. Burgos, P. Mattavelli, and Z. Shen, "Analysis of D-Q small-signal impedance of grid-tied inverters," *IEEE Trans. Power Electron.*, vol. 31, no. 1, pp. 675-687, Jan. 2016.

[25] L. Harnefors, X. Wang, A. G. Yepesand, and F. Blaabjerg, "Passivity-based stability assessment of grid-connected VSCs-an overview," *IEEE J. Emerg. Sel. Topics Power Electron.*, vol. 4, no. 1, pp. 116-125, Mar. 2016.

[26] C. Zhang, X. Cai, Z. Li, A. Rygg and M. Molinas, "Properties and physical interpretation of the dynamic interactions between voltage source converters and grid: electrical oscillation and its stability control," *IET Power Electron.*, vol. 10, no. 8, pp. 894-902, July. 2017.

[27] M. Belkhayat, "Stability criteria for ac power systems with regulated loads," *West Lafayette: Purdue University*, 1997.

[28] J. Sun and K. J. Karimi, "Small-signal input impedance modeling of line-frequency rectifiers. IEEE Transaction On Aerospace and Electronic Systems," *IEEE Trans. Aerosp. Electron. Syst.*, vol. 44, no. 4, pp. 1489-1497, Oct. 2008.

[29] L. M. Fernandez, F. Jurado, and J. R. Saenz, "Aggregated dynamic model for wind farms with doubly fed induction generator wind turbines," *Renew. Energy*, vol. 33, pp. 129-140, Jan. 2008.

[30] E. Muljadi and B. Parsons, "Comparing single and multiple turbine representations in a wind farm simulation," in *Eur. Wind Energy Conf.*, Athens, Greece, Jan. 2006, pp. 1-10.

[31] W. Tang, J. Hu, Y. Chang, X. Yuan, F. Liu, "Modeling of DFIG-based wind turbine for power system transient response analysis in rotor speed control timescale," *IEEE Trans. Power Syst.*, vol. 33, no. 6, pp. 6795-6805, Apr. 2018.

[32] J. Ying, X. Yuan, J. Hu, and W. He, "Impact of inertia control of DFIG-based WT on electromechanical oscillation damping of SG," *IEEE Trans. Power Syst.*, vol. 33, no. 3, pp. 3450-3459, Mar. 2018.

[33] I. Vieto and J. Sun, "Sequence impedance modeling and analysis of Type-III wind turbines," *IEEE Trans. Energy Convers.*, vol. 33, no. 2, pp. 537-545, Jun. 2018.

[34] I. Vieto and J. Sun, "Small-signal impedance modeling of type-III wind turbine," in *Proc. IEEE Power Energy Soc. Gen. Meeting*, Denver, CO, USA, Oct. 2015, pp. 1-5.

[35] B. Wen, R. Burgos, D. Boroyevich, P. Mattavelli, and Z. Shen, "AC stability analysis and DQ frame impedance specifications in power electronics based distributed power systems," *IEEE J. Emerg. Sel. Topics Power Electron.*, vol. 5, no. 4, pp. 1455-1465, Dec. 2017.

[36] S. Shah and L. Parsa, "Impedance modeling of three-phase voltage source converters in dq, sequence, and phasor domains," *IEEE Trans. Energy Convers.*, vol. 29, no. 5, pp. 1139-1150, Sept. 2017.

[37] A. Rygg and M. Molinas, "A modified sequence-domain impedance definition and its equivalence to the dq-domain impedance definition for the stability analysis of ac power electronic systems," *IEEE J. Emerg. Sel. Topics Power Electron.*, vol. 4, no. 4, pp. 1383-1396, Dec. 2016.

[38] A. Rygg, M. Molinas, C. Zhang, and X. Cai "On the equivalence and impact on stability of impedance modeling of power electronic converters in different domains," *IEEE J. Emerg. Sel. Topics Power Electron.*, vol. 5, no. 4, pp. 1444-1454, Dec. 2017.

[39] D. N. Zmood, D. G. Holmes, and G. H. Bode, "Frequency-domain analysis of three-phase linear current regulators," *IEEE Trans. Ind. Appl.*, vol. 37, no. 2, pp. 601-610, Apr. 2001.

Kun Sun received the B.S. and M.Sc. degrees in electrical engineering from Huazhong University of Science and Technology (HUST), Wuhan, China, in 2015 and 2018, respectively.

He is currently working toward the Ph.D. degree in electrical engineering at HUST. His current research interests include stability analysis and control of grid-integration of large-scale wind farm through VSC-HVDC.

Wei Yao (M'13-SM'17) received the B.S. and Ph.D. degrees in electrical engineering from Huazhong University of Science and Technology (HUST), Wuhan, China, in 2004 and 2010, respectively.

He was a Post-Doctoral Researcher with the Department of Power Engineering, HUST, from 2010 to 2012 and a Postdoctoral Research Associate with the Department of Electrical Engineering and Electronics, University of Liverpool, Liverpool, U.K., from 2012 to 2014. Currently, he has been an Associate Professor with the School of Electrical and Electronics Engineering, HUST, Wuhan, China. His current research interests include power system stability analysis and control, HVDC & FACTS, and renewable energy.

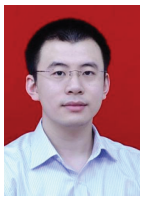

Jiakun Fang (S'10-M'13) received the B.Sc. and Ph.D. degrees from Huazhong University of Science and Technology (HUST), China, in 2007 and 2012, respectively.

He was with Huazhong University of Science and Technology (HUST), Wuhan, China. Currently he is an Associate Professor with the Department of Energy Technology, Aalborg University, Aalborg, Denmark. His research interests include power system dynamic stability control, power grid complexity analysis and integrated energy system.

Xiaomeng Ai (S'11-M'17) received the B.Eng degree in mathematics and applied mathematics and Ph.D. in electrical engineering in 2008 and 2014, respectively, both from Huazhong University of Science and Technology (HUST), Wuhan, China.

Currently he is a lecturer at HUST. His research interests include robust optimization theory in power system, renewable energy integration, and integrated energy market.

This article has been accepted for publication in a future issue of this journal, but has not been fully edited. Content may change prior to final publication. Citation information: DOI 10.1109/JESTPE.2019.2901747, IEEE Journal of Emerging and Selected Topics in Power Electronics

Jinyu Wen (M'10) received the B.S. and Ph.D. degrees in electrical engineering from Huazhong University of Science and Technology (HUST), Wuhan, China, in 1992 and 1998, respectively.

He was a Visiting Student from 1996 to 1997 and Research Fellow from 2002 to 2003 all at the University of Liverpool, Liverpool, UK, and a Senior Visiting Researcher at the University of Texas at Arlington, Arlington, USA, in 2010. From 1998 to 2002 he was a Director Engineer with XJ Electric Co. Ltd. in China. In 2003, he joined the HUST and now is a Professor with the School of Electrical and Electronics Engineering, HUST. His current research interests include renewable energy integration, energy storage, multi-terminal HVDC and power system operation and control.

Shijie Cheng (M'86-SM'87-F'11-LF'18) received the B.S. degree from Xi'an Jiaotong University, Xi'an, China, in 1967, the M.Sc. degree from Huazhong University of Science and Technology (HUST), Wuhan, China, in 1981, and the Ph.D. degree from the University of Calgary, Calgary, AB, Canada, in 1986, all in the electrical engineering.

He has been a Professor with the School of Electrical and Electronics Engineering, HUST, Wuhan, China, since 1991. His research interests are power system control, stability analysis, application of Artificial Intelligence, and energy storage.

Prof. Cheng is a Fellow of the Chinese Academy of Sciences.